

8

Interferometer Performance and Characterization

8.1 RANDOM AND SYSTEMATIC ERROR MEASUREMENT	142
8.2 REFERENCE PINHOLE SPATIAL FILTERING	142
8.3 OBJECT PINHOLE SPATIAL FILTERING	144
8.4 THROUGH-FOCUS EXPERIMENTS	145
8.5 MECHANICAL STABILITY: DRIFT	147
8.6 OBJECT PINHOLE EXCHANGE AND MEASUREMENT REPEATABILITY	141
8.6.1 Multiple Object Pinholes	
8.6.2 System Re-Alignment	
8.7 TEMPERATURE MEASUREMENT	150
8.8 ZERO-ORDER REFERENCE VERSUS FIRST-ORDER REFERENCE	151
8.9 OBSERVATION OF THE GEOMETRIC COMA SYSTEMATIC ERROR	152
8.10 PHASE-SHIFTING ANALYSIS	154
8.10.1 Phase-Calibration Difficulties	
8.10.2 Comparison of Phase-Shifting Methods	
8.10.3 Fourier-Transform versus Phase-Shifting Methods	
8.10.4 Sensitivity of Least-Squares Phase-Shifting Analysis	
8.10.5 Intensity Fluctuations	
8.11 FRINGE CONTRAST AND WAVEFRONT FITTING UNCERTAINTY	161
8.12 SUMMARY AND CONCLUSIONS	162
8.12.1 Summary of Precision-Testing Measurements	
8.12.2 Comments	
8.12.3 The Astigmatism Problem	
8.12.4 Accuracy and the Need for <i>Two Pinhole Tests</i>	

8.1 RANDOM AND SYSTEMATIC ERROR MEASUREMENT

This chapter describes a number of experiments that are performed to characterize the magnitude and effect of random and systematic errors on the performance of the interferometer. Of the random errors, the most significant stem from the spatial filtering of the reference wavefront by the reference pinhole and the spatial filtering of the illumination wavefront by the object pinhole. Direct measurements of these effects place bounds on the system's sensitivity to alignment.

In principle, each optical component of the interferometer is capable of introducing its own systematic error into the wavefront measurements. Both mechanical and optical concerns are paramount. Experiments (described here) are performed to assess the mechanical and thermal stabilities of the system. Systematic errors potentially contributed by the grating beamsplitter are investigated in the comparison of the zero-order reference to the first-order reference PS/PDI configurations. As an indication of the sensitivity of the wavefront measurements, the geometric coma systematic error is examined.

Finally, the analysis methods themselves are investigated: the performance of the complex methods described in Section 12.5 is compared to the conventional, simple methods described in Section 12.2. The Fourier-transform method (Section 11.3) is also compared to the phase-shifting analyses.

In many of the experiments described in this section, the Fourier-transform method of single interferogram analysis is used to extract the wavefront from individual measurements. In nearly all cases described here, the uncertainties introduced by this analysis method are significantly smaller than the effects being measured. Furthermore, fitting the resultant wavefront data to the Zernike polynomials (Chapter 15) reduces noise and high-frequency variations in the data.

8.2 REFERENCE PINHOLE SPATIAL FILTERING

It is known that pinhole size affects the quality of the reference wavefront. While theoretical calculations help to establish the relationship between pinhole size and predicted wavefront quality, the *actual* quality of the spatial filtering can only be assessed *in situ*. One simple way to perform such measurements is by the intentional misalignment of the reference pinhole about the focus of the reference beam. An ideal spatial filter produces a spherical wavefront regardless of how it is illuminated. Experimentally, however, it has been shown that the alignment *does affect* the wavefront measurements. This is not at all unexpected, considering the fact that measured reference pinhole sizes (Section 6.4.2) are larger than the sub-100-nm target size.

Presently, when the interference patterns are recorded fine alignment is performed to optimize the appearance of the fringes, as judged by the operators of the interferometer. Hence, it may be said that the position of the pinhole is arbitrary within a small domain of positions that produce analyzable and reason-

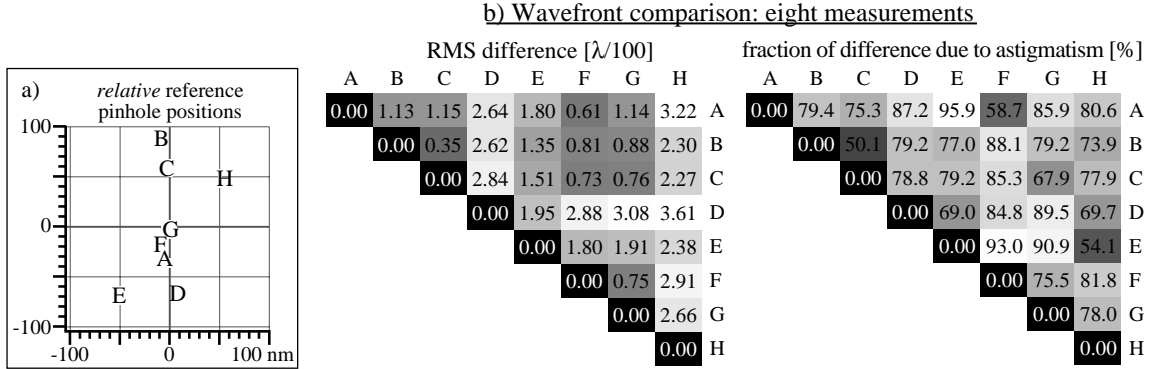


Figure 1. Assessment of the spatial-filtering properties of the reference pinholes is performed by comparing the interferometrically-measured wavefront recorded at several de-optimized pinhole positions within the focus of the reference beam. (a) Small translations produce a measurable change of tilt, allowing the arbitrary *relative* positions of the pinhole to be determined. (b) Analysis of the *difference wavefronts*, computed for all pairs of measurements, indicates the expected variability or uncertainty in the wavefront measurements. The largest reported RMS displacement values of the difference wavefront are on the order of $\lambda/30$ and the average value is 0.0186 waves. Most of the RMS difference comes from the astigmatic component. The fraction of the RMS related to astigmatism is also shown. Experimental wavefront variations are expected to be smaller than these values because the reference pinhole position is optimized before measurement.

ably high-quality interferograms. Intentional translation of the pinhole to positions within this small domain gives a qualitative assessment of how sensitive the wavefront measurements are to the position of the reference pinhole.

To establish an upper bound on the wavefront uncertainty, the reference pinhole is moved as far from the optimum as possible without losing the fringe pattern. Experimental uncertainties may thus not be this large in practice.

Figure 1 shows the results of this test as performed using Pinhole D and the 0.07 NA sub-aperture A. The reference pinhole was moved to eight separate arbitrary positions and a single interferogram was recorded at each. Analysis was performed using the Fourier-transform method of single interferogram analysis with a Gaussian filter $1/e^2$ radius of 8 cycles in the spatial-frequency domain. The eight measured wavefronts, labeled A through H, were compared, with the piston, tilt, and defocus terms subtracted. The RMS displacement of the *difference wavefronts* are shown in Fig. 1 for each pair. The largest difference is 0.0361 waves (0.484 nm, or $\sim\lambda/28$); the average measured difference among all of the comparisons is 0.0186 ± 0.0093 waves (0.249 nm, or $\sim\lambda/53$).

The relative positions shown in Fig. 1(a) are inferred from the measured tilts and an assumed measurement NA of 0.066 (based on the 0.07 NA sub-aperture and the size of the sub-region used for analysis). The positions are determined from an easily-derived expression: with small NA, the path length difference ΔR is

$$\Delta R[\lambda] = \frac{NA}{\lambda}(x, y) \cdot (Z_1, Z_2). \quad (1)$$

Z_1 and Z_2 are the Zernike polynomial x - and y -components of the tilt, and (x, y) is the lateral displacement vector. The distribution width of these points indicates that the largest tolerable pinhole displacements are on the order of 175 nm.

The wavefront variation shown here indicates that from any *single* interferogram measurement, an uncertainty of approximately 0.02 waves RMS (0.268 nm, or $\lambda/50$), should be expected. Since the reference pinhole position in the beam is adjusted before each series of measurements, this uncertainty becomes a random error source. The implications of this result for phase-shifting measurements, which incorporate several (typically 5) interferograms together in a single measurement, are not clearly discernable.

Inspection of the individual difference wavefronts reveals that the dominant aberration component is always astigmatism. In general, the disagreements between any two measured wavefronts are dominated by variations in the measured astigmatism. The fraction of astigmatism in the RMS differences is shown in Fig. 1(b) for each measurement pair. These fractions are between 50 and 96%, with most above 75%. This astigmatism problem is discussed in Section 8.13.3.

8.3 OBJECT PINHOLE SPATIAL FILTERING

A similar set of experiments can be performed to assess the quality of the spatial filtering performed by the object pinhole in generating a spherical illuminating wavefront. By incorporating alignment positions far from the optimum, these simple tests provide an upper bound on the expected measurement uncertainty. Although variations from only one component are of interest, these experiments involve two components of the interferometer. When the object pinhole is displaced laterally, the position of the reference beam focus in the image-plane also moves. The sensitivity of the wavefront measurements to the position of the reference pinhole, demonstrated in Section 8.2, necessitates re-optimization of the reference pinhole position for each measurement. Thus there is no simple way to isolate the effect of the object pinhole alone.

These tests were performed using sub-aperture A. The results of two object pinhole displacement experiments are shown in Fig. 2. Once again, the Fourier-transform method of single interferogram analysis is used (Section 8.2). The intensity in a lateral plane near the K-B focus is measured by scanning the object pinhole, using a photodiode to record the transmitted flux at each position. In each test, five object pinhole positions (A through E) are sampled, as shown in the Fig. 2. The stage is calibrated and the positions are known to within 1 μm . As before, the RMS displacement of the *difference wavefronts* are calculated for each pair of measurements, with piston, tilt, and defocus terms removed.

For Test #1, the average RMS difference is 0.0061 ± 0.0013 waves (0.0819 ± 0.0178 nm, or $\sim\lambda/164$). For Test #2, the average is 0.0143 ± 0.0049 waves (0.1918 ± 0.0654 nm, or $\sim\lambda/70$). Since the object

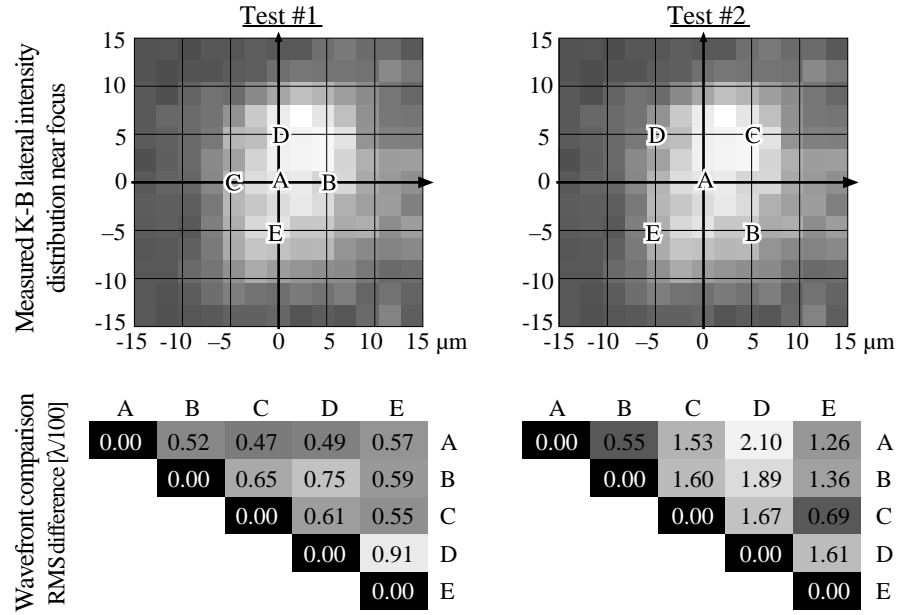


Figure 2. To assess the quality of the object pinhole spatial filter, two separate experiments were performed in which the object pinhole was translated laterally in the vicinity of the K-B focus. (Above) The positions within the measured K-B intensity profile are indicated by the letters A through E in each test. For each measurement, the position of the reference pinhole was re-optimized and the wavefront was calculated. (Below) Comparisons of the wavefront measurement pairs, with piston and tilt removed, are shown in terms of the RMS displacement of the difference wavefronts. The discrepancy in the typical difference-magnitudes observed within each test is attributable to the fact that different object and reference pinholes were used in each case.

pinhole position is seldom adjusted during the course of many measurements, this uncertainty enters the experiment as a systematic error source. In practice, the actual wavefront variation will be much smaller than the wavefront variation caused by the intentional displacement of the object pinhole.

8.4 THROUGH-FOCUS EXPERIMENTS

An important test of the spatial filtering properties of the object pinhole is one that examines the dependence of the measured wavefront on the longitudinal, or *focal*, position of the object pinhole. Because the reference pinhole remains stationary in the image-plane, translating the object pinhole causes only the test beam to focus above or below the image-plane.

Since the window is very large compared to the focal spot diameter, within a broad range of focal positions the window transmits the test beam with almost no dependence on the focal position. The tiny reference pinhole, however, defines a stationary center-of-curvature for the reference beam. Thus with their longitudinal centers-of-curvature displaced, the test and reference beams acquire a small amount of *defocus*. The defocus magnitude is easily derived for small NA. In waves, the path-length-difference is

$$\Delta R[\lambda] = \frac{z NA^2}{4\lambda} Z_3. \quad (2)$$

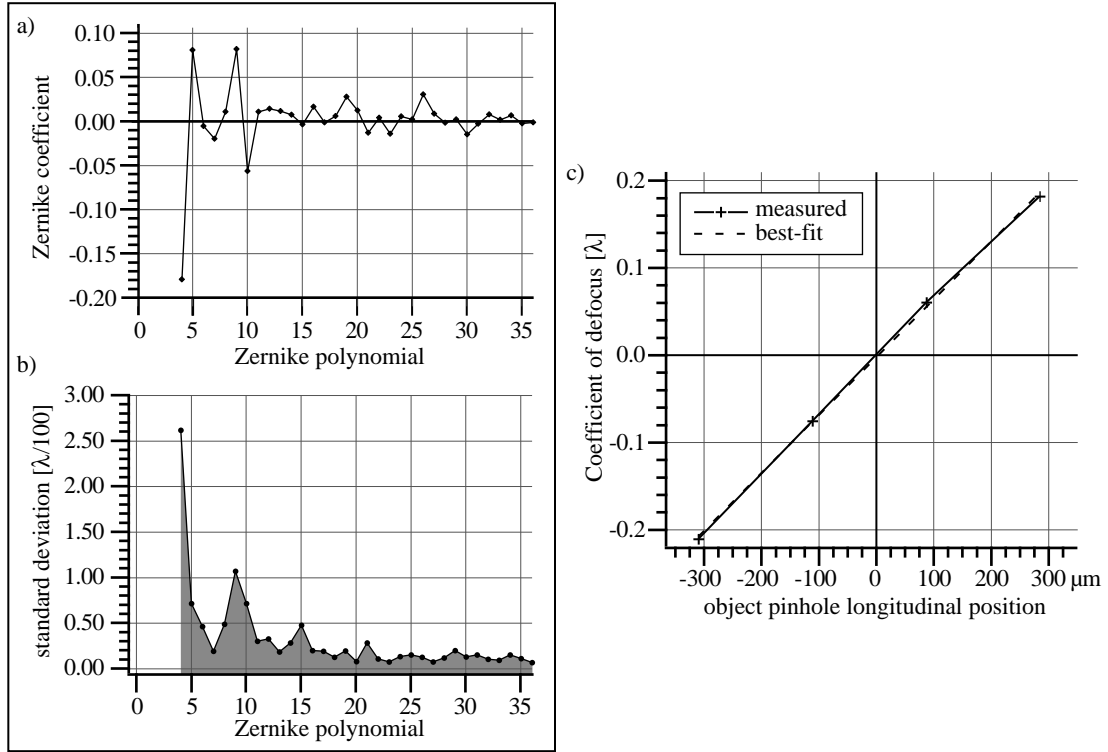


Figure 3. Wavefront measurements recorded as the longitudinal position of the object pinhole is adjusted are used to assess the sensitivity of the system to defocus. For each measurement, the position of the reference pinhole was also re-optimized. (a) A comparison of the Zernike polynomial fits to the four measured wavefronts shows excellent agreement of the aberration coefficients. (b) The magnitude of the differences in these coefficients is shown. The longitudinal position is known via the calibrated stage and the measured defocus, which depends linearly on the longitudinal position. (c) The measured defocus follows the longitudinal position linearly, as expected. However, the slope indicates a *measurement NA* of 0.060 on the image-side, which is smaller than expected.

z is the longitudinal displacement, and Z_3 is the Zernike polynomial corresponding to defocus.

Figure 3 contains the results of this experiment, again performed using sub-aperture A. The object pinhole was translated vertically by a total of 594.5 μm , and four individual interferogram measurements were made. Here, as in Section 8.3, the experiments require re-optimization of the reference pinhole after each longitudinal translation. Thus the added uncertainty introduced by the reference pinhole effects are incorporated in these results. Figure 3(a) shows the average of the measured Zernike polynomial coefficients, excluding piston, tilt, and defocus. The very small standard deviations of each term (determined by the four measurements) are shown in Fig. 3(b).

Figure 3(c) shows the measured Zernike coefficient of defocus versus the longitudinal position of the object pinhole and reveals a discrepancy in the measurement. The slope of the best-fit line is 6.626×10^{-4} waves/ μm . Using Eq. (2), at 13.4 nm wavelength, this slope indicates a measurement NA of 0.0060 on the object side or 0.060 on the image-side. Based on the maximum width of the illuminated area in the recorded data (702 pixels) and on the size of the circular sub-region used for analysis (659 pix-

els), the predicted *measurement NA* is 0.066 within this “0.07 NA sub-aperture.” At the time these experiments were conducted, the NA was not accurately known from other means; it is therefore possible that the numerical apertures under consideration are actually smaller than expected, by as much as 9%.

8.5 MECHANICAL STABILITY: DRIFT

Care was taken to design the interferometer to be rigid and isolated from vibration. Separate from the motions of the source and the beamline, the most critical positions are the *relative* locations of the object pinhole with respect to the Schwarzschild test optic and of the image plane pinholes. Recalling that the image-plane pinholes are mounted to the test optic, the most likely source of drift in the system is the position of the object pinhole with respect to the test optic. Clearly, the best way to measure the importance of drift in the interferometer system, and probably in *any* interferometer system, is to observe changes in the measured wavefront *in situ*.

Several such experiments were performed; the results of one are shown in Fig. 4. Here, the positions of the pinholes and the test optic are optimized and then not adjusted for ten minutes. A single interferogram measurement is made once every two minutes for a total of six measurements; each wavefront is compared

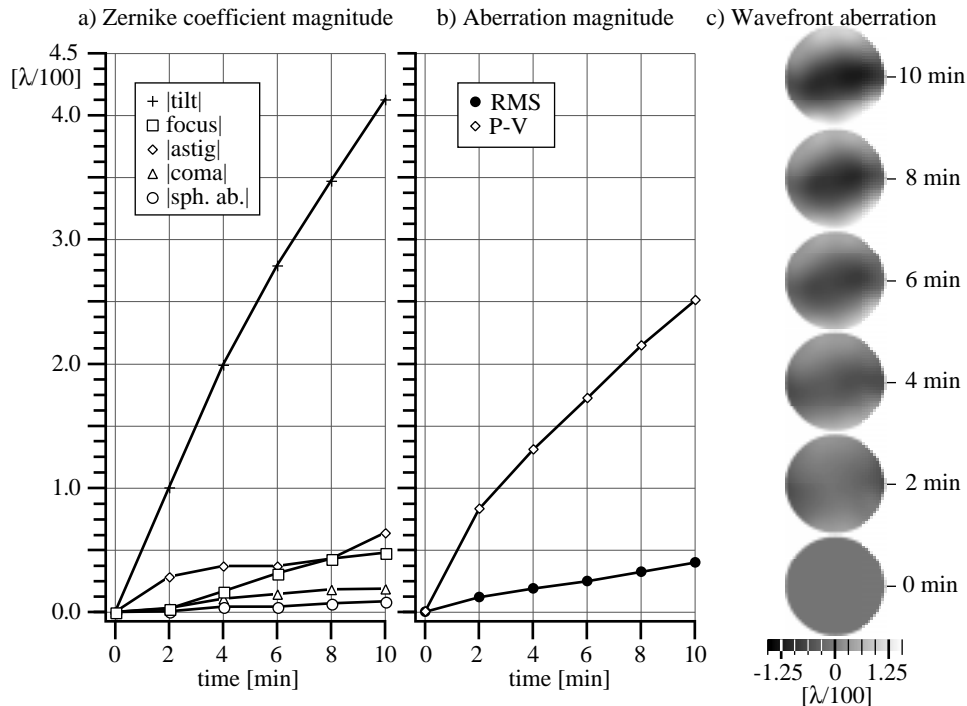


Figure 4. *In situ* measurement of mechanical stability is performed by observing changes in the measured wavefront over time, as the system is left undisturbed in one position. Changes are recorded with respect to the first measured wavefront (time = 0 min). (a) The magnitude of the change in tilt indicates a lateral drift of approximately 90 nm in 10 minutes. (b) With the tilt component removed from the analysis, the RMS and P-V displacements of the measured wavefronts are also shown. In ten minutes, the RMS difference did not exceed $\lambda/200$. (c) The difference wavefronts are plotted using a consistent grayscale.

to the first. The wavefronts are calculated using the Fourier-transform method with a narrow Gaussian filter $1/e^2$ width of four cycles in the spatial-frequency domain. The Zernike coefficient magnitudes of the primary aberrations in the difference wavefronts are shown in the Fig. 4(a): by definition, the P-V error from any of these is twice the magnitude of the coefficient. The P-V and RMS wavefront displacements are shown in Fig. 4(b) with the piston and tilt terms removed.

Following Eq. (1), and using the NA value from the defocus experiment (Section 8.4), the measured 4.1×10^{-2} waves of tilt indicate a lateral drift of approximately 90 nm in 10 minutes, or 9 nm/min on the image-side of the optic. The defocus coefficient reached a maximum value of 4.8×10^{-3} waves, which by Eq. (2) indicates a longitudinal shift of 7.2 μm in 10 minutes, or 0.72 $\mu\text{m}/\text{min}$ on the object-side of the system.

To correctly replicate the way in which the interferometer has been used, the system was *not* allowed to stabilize after the alignment had been optimized. It is possible that the system drifts most rapidly immediately after it is adjusted, and then reaches a more stable position. Further investigations to characterize the system drift are warranted, but have not yet been performed. The maximum allowable drift rate should be based on the rate of data collection, and on the target accuracy of the measurements.

An important secondary result can also be extracted from this experiment. The clear observation of small, well-behaved incremental changes using single-interferogram analysis methods indicates the high sensitivity of this interferometer, with measurement precision below $\lambda/100$. This precision magnitude is supported by other self-consistency tests described in Section 8.10.3.

8.6 OBJECT PINHOLE EXCHANGE AND MEASUREMENT REPEATABILITY

Understanding the performance of the interferometer and the qualities of its components requires evaluation of the wavefront measurements, subject to the exchange of “identical” elements wherever possible. To what extent do the measurements depend on the optical components separate from the optic under test? By performing a series of experiments with a number of different object pinholes, for example, systematic errors potentially introduced by defects in any one pinhole become random errors in the larger data set.

This section describes two important experiments designed to evaluate the object pinholes and the importance of system alignment. Because re-alignment was performed during the evaluation of the multiple-pinhole effects, the results of these two experiments are essentially coupled.

8.6.1 Multiple Object Pinholes

More than seven individual object pinholes were used in interferometry experiments. Two pinholes were known to be too large to fill the measurement NA; those measurements are not presented in this section. Five other pinholes, discussed here, are commercially available laser-drilled pinholes designed to be

0.5- μm in diameter. They may in fact be somewhat larger.

One object pinhole was used for numerous measurements of sub-aperture A, referred to here as the “March” data (these experiments were performed in March of 1997). After the March data were recorded, the Schwarzschild objective was re-aligned for measurement of sub-apertures B and C. Then the system was returned to sub-aperture A for repeatability studies. In this position, the “April” data were recorded. Here four different object pinholes were used, not including the pinhole used for the March data.

All of the measurements correspond to sub-aperture A, and were performed using the same image-plane reference pinholes and window. For each pinhole under consideration, all available measurements were combined to form a single set of Zernike polynomial coefficients.

The agreement among the five measurements is presented in Fig. 5. Figure 5(a) shows a plot of the Zernike coefficients measured with each of the five pinholes. The five pinholes are labeled A through E. A alone represents the March data, and B through E represent the April data. The variation in the measured wavefronts is described by the *difference wavefront* statistics calculated for each pair of measurements. Tables of the

RMS and P-V displacements of the difference wavefronts are shown in Fig. 5(b).

Examining the P-V measurements, one trend is apparent: the agreement is generally better among B through E than it is between A and any of the others. One explanation is the system re-alignment, addressed in the following section. The RMS displacements are all on the order of 0.01 to 0.02 waves, consistent with the variation seen in the reference pinhole displacement experiment, described in Section 8.2.

8.6.2 System Re-Alignment

As described above, the Schwarzschild objective was removed from the interferometer chamber and reinstalled several times, including once for each of the three sub-apertures tested. At the time these experiments were conducted, the optic was not kinematically mounted to the translation-stage that controlled its

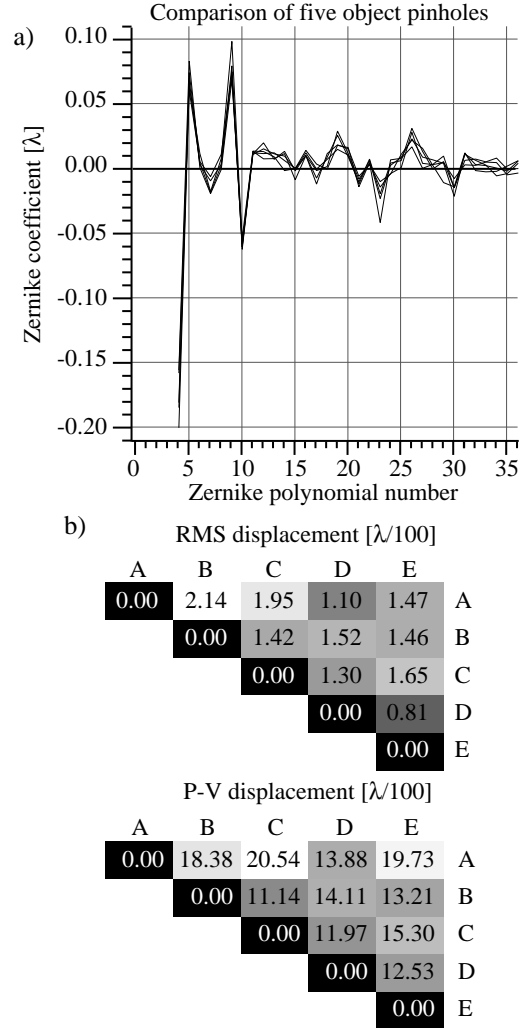


Figure 5. Comparison of wavefront measurements under the exchange of five “0.5- μm ” object pinholes. (a) The Zernike polynomial coefficients and (b) the RMS and P-V displacements of the difference wavefronts are shown. Uncertainties are consistent with other measurements requiring re-optimization of the reference pinhole position.

lateral movement, and the range of stage motion was very limited. (These problems have since been addressed.) This re-alignment procedure required several iterations to bring the position, rotation, and angle of the test optic and the position and angle of the EUV beam into an optimum configuration. A comparison of measurements made before and after re-alignment demonstrates the repeatability of the measurements, as performed from scratch.

As described in the previous section, the comparison between the March and April data (i.e., the comparison of the measurements made before and after re-alignment) was performed using a number of object pinholes. This adds an extra degree of uncertainty to the difference measurement and further explains why this experiment is coupled to the pin-hole exchange experiment.

The comparison is shown in Fig. 6. The two overlapping sets of Zernike polynomial coefficients are shown in 6(a); 6(b) shows the magnitude of the difference. Here the only terms larger than $\lambda/100$ are astigmatism Z_4 and the ninth Zernike polynomial, Z_9 , which is *triangular astigmatism*. These are also the two aberration components with the largest Zernike polynomial coefficients. The RMS and P-V displacements of the difference wavefront are, respectively, 0.018 and 0.153 waves (0.24 and 2.05 nm, or $\sim\lambda/56$ and $\sim\lambda/6.5$). Seventy-four percent of the RMS difference comes from the astigmatic component alone.

8.7. TEMPERATURE MEASUREMENT

An experiment was conducted to gauge the thermal stability of the interferometer chamber over two days of typical operation. The air inside the experimental area of the Advanced Light Source where the interferometer sits is designed to be controlled to $\pm 0.5^\circ\text{C}$. However, the experimental system sits within 10 m of a large access door that is opened several times per day for several minutes at a time. Concern over the actual chamber temperature prompted this simple study.

A temperature meter was placed in thermal contact with the base of the interferometer chamber and the temperature was recorded intermittently for two days. The results, shown in Fig. 7, verify that the chamber temperature stays within the published specifications of the ALS experimental floor. Additional tempera-

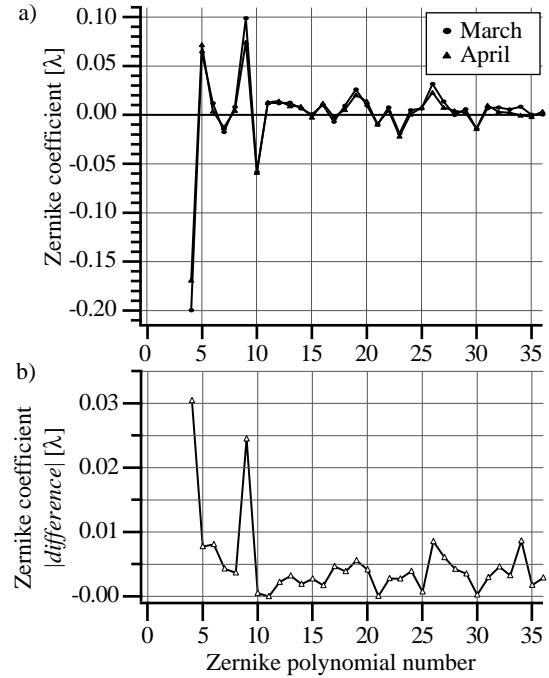


Figure 6. Measurements recorded before and after a complete system re-alignment show excellent agreement. Measurements are also separated by more than two weeks. A comparison (a) of the Zernike polynomial coefficients and (b) the magnitude of their difference.

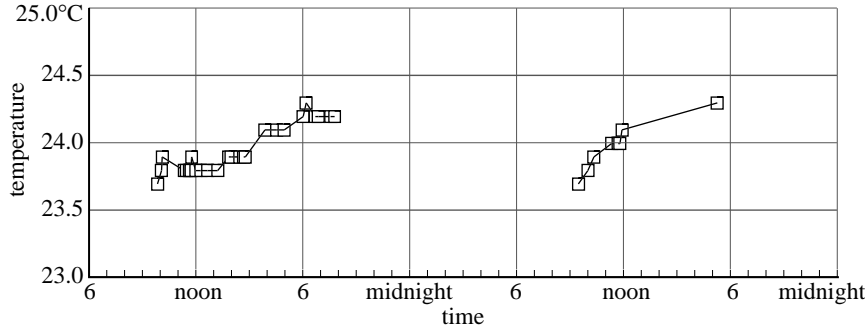


Figure 7. The temperature of the interferometer chamber wall was sampled over a two-day period. These and other measurements (not pictured) show stability to within $\pm 0.5^\circ\text{C}$ with a slow daily rise and nightly fall in temperature.

ture measurements have since been conducted in which the temperature from a number of probes in various positions is recorded automatically at regular intervals. The newer measurements are in good agreement with the data shown here.

8.8 ZERO-ORDER REFERENCE VERSUS FIRST-ORDER REFERENCE

A small number of experiments were conducted to measure the difference between the *zeroth-order reference* and the default *first-order reference* configurations of the interferometer. These two very similar modes of operation are defined in Section 4.3 and discussed further in Sections 5.4, 5.8.4, and 5.10. As the names imply, the essential difference is a reversal-of-roles changing which one of the beams from the grating beamsplitter is used as the test beam and which one as the reference beam. By definition, the reference beam is that beam which is brought to focus on the reference pinhole to produce the spherical reference wavefront. Starting in the first-order reference position, a simple $4.5\text{-}\mu\text{m}$ translation of the beam positions in the image-plane brings the zeroth-order beam to focus on the reference pinhole; the *other* first-order beam becomes the test beam.

From a typical, binary transmission grating, the first-order beams are each 40% as intense as the zeroth-order. Spatially filtering a first-order beam in the first-order reference configuration *increases* the intensity discrepancy between the test and reference beams and further reduces the fringe contrast. Evidence of the improvement in fringe contrast offered by the zeroth-order reference configuration is shown in Figs. 8(a) and 8(b). Improved fringe contrast facilitates the analysis.

While intensity-balancing issues motivate the use of the zeroth-order reference configuration, concern for the quality of the grating's diffracted first-order beam is paramount. For this reason, the first-order reference configuration, which filters the diffracted beam, became the default mode of operation.

A comparison of the same wavefronts measured in both configurations is given in Fig. 8(c). Here, the RMS displacements of the difference wavefronts are all less than or equal to 0.0131 waves (0.176 nm, or $\sim\lambda/76$). Because reference pinhole re-alignment is required in each case, the uncertainties in these measurements do include the reference pinhole alignment uncertainty discussed in Section 8.2. Since that

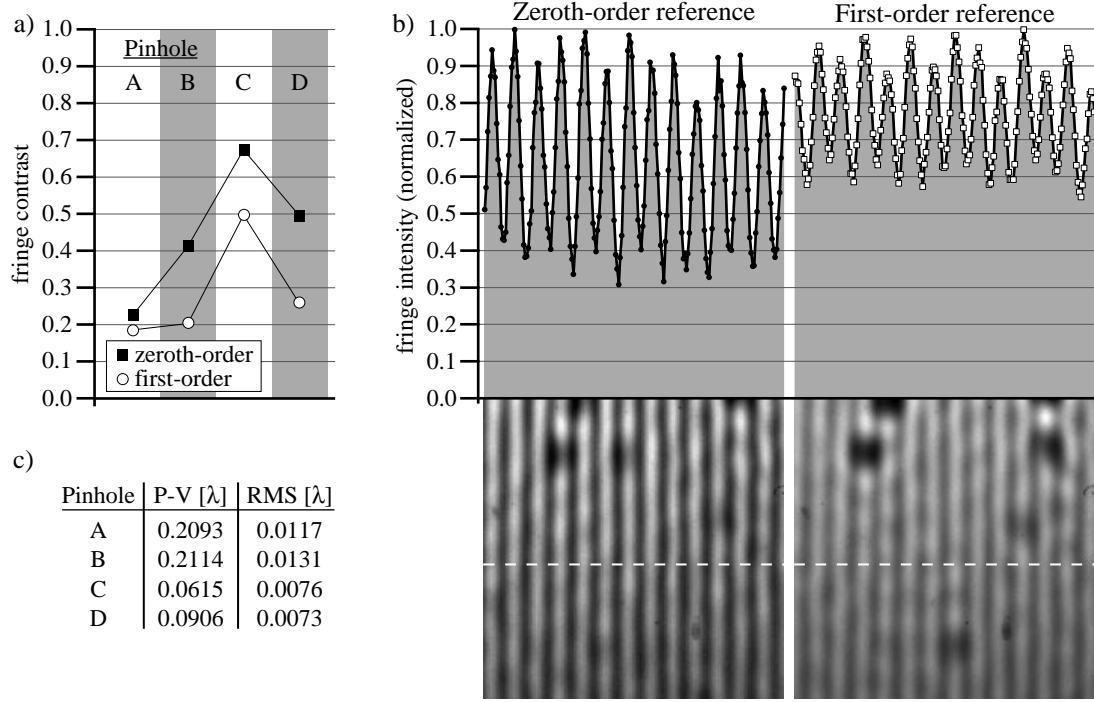


Figure 8. A comparison of wavefronts measured using the default first-order reference and the zeroth-order reference configurations of the PS/PDI. While the first-order reference configuration uses the zeroth-diffracted-order beam from the grating to ensure a high-quality test beam, the zeroth-order reference configuration offers a significant improvement in fringe contrast by balancing the intensities of the two beams more closely. (a) From each of the four pinholes (A, B, C, and D), the fringe contrast is shown for both configurations. (b) For a comparison, one typical sub-region of the interferogram pattern is shown in detail. The cross-sections taken from the position of the dashed white line reveal both the fringe modulation and the sampling density of the raw data. (c) The RMS and P-V displacements of the difference wavefronts show that the phasemap measurements are nearly indistinguishable within typical measurement uncertainties.

uncertainty is larger than the discrepancy found in this study, it is thus possible that the magnitudes of the wavefront differences between these two configurations are below the measurement uncertainty.

8.9 OBSERVATION OF THE GEOMETRIC COMA SYSTEMATIC ERROR

The small ($4.5 \mu\text{m}$) image-plane displacement of the test and reference beam centers-of-curvature introduces a geometric coma systematic error that is readily observable in the data (Section 5.5). The clear observation of this very small effect serves to demonstrate the high resolution of the EUV PS/PDI.

The magnitude and direction of the coma systematic error depend linearly on the beam separation. When an isolated wavefront measurement is made, the contribution of this systematic error is unknown. However, when any two such measurements are performed with a rotation or change in the separation, the *wavefront difference* between the two measurements reveals the isolated contribution of the systematic error.

The PS/PDI image-plane spatial filter was designed to facilitate the removal of this systematic error. By performing *two* wavefront measurements using reference pinholes placed 90° apart with respect to the window, the geometric coma is easily identified and removed according to the prescription

Table 1. Difference wavefront statistics from measurements performed in two nearly orthogonal directions. Tilt (\mathbf{T}_Δ) and coma (\mathbf{C}_Δ) for sub-apertures A and C.

Sub-aperture	$ \mathbf{T}_\Delta $		$ \mathbf{C}_\Delta $	
	P-V	$\theta_{\mathbf{T}}$	P-V	$\theta_{\mathbf{C}}$
A	62.94 $\lambda = 843.3$ nm	46.48°	0.068 $\lambda = 0.92$ nm	45.77°
C	55.41 $\lambda = 742.5$ nm	46.81°	0.017 $\lambda = 0.23$ nm	46.89°

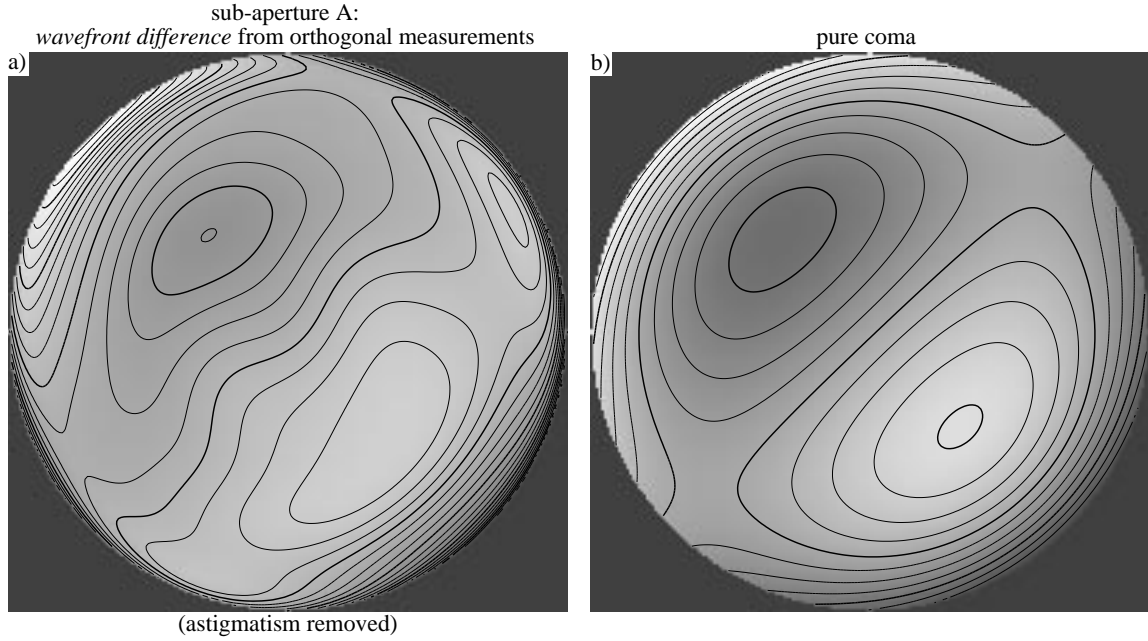


Figure 9. Observation of the geometric coma systematic error can be made by the subtraction of any two measurements in which the beam separation has changed. With the beam separation, and hence the coma, rotated by nearly 90°, the *difference wavefront* shows the coma effect at approximately 45°. Data from sub-aperture A (a) is shown alongside pure coma (b) for comparison. Because the variation of the astigmatism term masks this small effect (less than 1 nm in a 0.07 NA sub-aperture), astigmatism has been subtracted from this figure. The variations in (a) are related to the measurement uncertainties.

described in Section 5.5.2.

The magnitude of the systematic error is small. For the measured difference wavefronts, the *tilt difference vector* \mathbf{T}_Δ and the *coma difference vector* \mathbf{C}_Δ are shown in Table 1. Within each sub-aperture, \mathbf{T}_Δ and \mathbf{C}_Δ are expected to be parallel; the angles $\theta_{\mathbf{T}}$ and $\theta_{\mathbf{C}}$ shown in the table demonstrate the agreement with expectations.

Based on measurements from sub-aperture A, Fig. 9(a) shows a difference wavefront obtained by subtracting the average wavefronts measured in the two nearly orthogonal beam separation directions. Because this effect is small relative to the variation in the measured astigmatism, the astigmatism has been removed from the difference wavefront in the creation of this figure. For comparison, Fig. 9(b) shows a *pure* coma aberration aligned in the direction of $\theta_{\mathbf{T}}$.

While the measurements presented for sub-aperture A represent the average of nineteen separate phase-shifting series, those for sub-aperture C come from only *two* measurements, one series in each direc-

tion. Given the small size of the data set, the level of agreement in the difference tilt and coma angles is remarkably high. This agreement both facilitates the removal of the systematic coma and emphasizes the high precision of the individual measurements.

8.10 PHASE-SHIFTING ANALYSIS

Analysis of the EUV phase-shifting PS/PDI data proved to be extremely complicated due to the unreliable positioning of the grating translation stages responsible for controlling the phase-shifting increments. To overcome these difficulties, the author developed the *Fourier-Transform Method of Phase-Shift Determination* (Section 12.4.2) and applied it using the least-squares method of phase-shifting analysis (Section 12.2.3). This section explains the necessity of this new technique and demonstrates the advantages of this method over others, using experimental data. Several available phase recovery techniques for phase-shifting methods of analysis are presented in Chapter 12, along with a discussion of specific advantages and limitations of each. The inherent sensitivity of the least-squares method of phase-shifting analysis is presented at the end of this section, and the implications for polynomial fitting uncertainties are discussed.

8.10.1 Phase-Calibration Difficulties

Difficulty in guaranteeing the position of the PS/PDI grating beamsplitter stages plagued the phase-shifting analysis of the interferometric data during the entire course of measurements. For each individual phase-shifting measurement, a series of five to nine (most often, five) interferograms was recorded. After each exposure, the position of the grating was advanced by approximately one-quarter cycle, or $4.5\ \mu\text{m}$ of its $18\text{-}\mu\text{m}$ pitch. The stage motion is calibrated *in situ* by careful observation of the fringe pattern during the motion of the stage over more than 20 cycles ($360\ \mu\text{m}$) of motion. During the measurement of a phase-shifting series, the grating is translated by only one to two cycles total, depending on the number of exposures.

From *all* of the phase-shifting measurements, 951 individual interferograms, or 163 phase-shifting series, were investigated to determine the magnitude of the phase-step errors. The relative *overall phase* of each image was calculated using

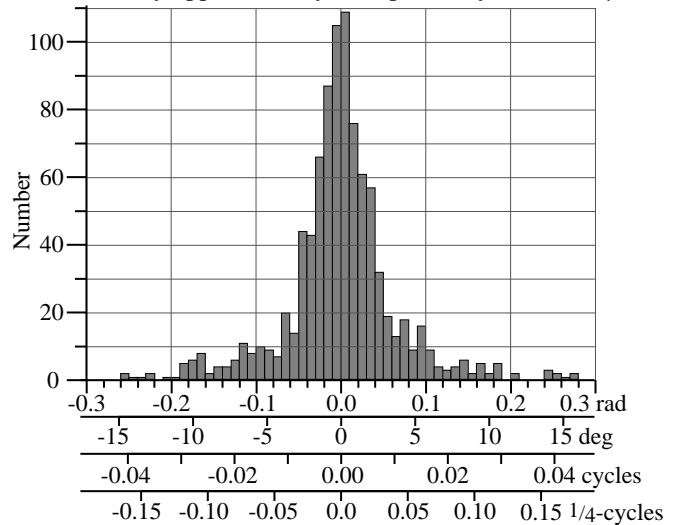


Figure 10. Histogram of phase-step errors, calculated using 927 interferograms, from 163 separate phase-shifting series. Limitations in the grating translation stage lead directly to errors in the phase-increments. The target increment was always one quarter-cycle, or $\pi/2$. The global phase of each interferogram was calculated using the Fourier-Transform Method of Phase-Shift Determination.

the Fourier-Transform Method of Phase-Shift Determination (Section 12.4.2). Then *within* each series the average phase *increment* was subtracted and the distribution about the mean phase-increment was tabulated. A histogram of the phase-step errors is shown in Figure 10. Here the ordinate is given in radians, degrees, cycles, and quarter-cycle steps (the target increment). The full-width at half-maximum of this distribution is approximately 0.07 radians, 4.0 degrees, 0.011 cycles, or 4.4% of the quarter-cycle step.

8.10.2 Comparison of Phase-Shifting Methods

Evaluation of the available methods of phase-shifting analysis using experimental EUV data is the most appropriate way to discern the actual benefits and drawbacks each. To illustrate such an investigation, a single phase-shifting measurement series was selected. This series is comprised of nine exposures with an (unintentionally) irregular phase-increment. Elements of this study are shown in Fig. 11. Using data from sub-aperture B, a relatively-clear 160×160 pixel sub-region was chosen. Details of four phase-shifted exposures are shown.

The Fourier-Transform Method of Phase-Shift Determination was used to determine the global phase-shift between exposures. Here, the complex phase of the first-order peak in the spatial-frequency spectrum is used to assign a global phase to the interferogram. The average phase increment was found to be 88.0° . The individual steps or step errors are shown in Fig. 11(b).

Seven separate methods of phase-shifting analysis are applied to the raw data. The unwrapped phasemaps from each method are shown with the piston and tilt components removed. The four-step method (Section 12.2.1) uses only the first four exposures. The Hariharan method (Section 12.2.2), utilizing the first five exposures, is applied in two different ways: first, assuming quarter-cycle steps, and second, using the known average 88° phase increment. A nine-step method* was the last of the *simple* methods to be applied. The complex method is applied in three ways, using the global phase increments calculated with the Fourier-Transform Method of Phase-Shift Determination. The least-squares method was applied to three, five, and then all nine exposures.

One characteristic feature exemplifies the main problem associated with the simple techniques: in the presence of phase-step errors, ripples appear in the data at twice the frequency of the fringe pattern. This so-called *fringe print-through*, clearly visible in the first four images of Fig. 11(c), is absent from the three applications of the complex method.

The discrepancies between the individual methods are most clearly revealed in the *difference wavefronts* calculated by subtracting the phasemap of the nine-bucket least-squares algorithm from the

* A *nine-step* phase-retrieval algorithm developed by the author. Quarter-cycle steps are assumed.

$$\phi(\mathbf{x}) = \tan^{-1} \left[\frac{2(I_4 - I_6 + I_8 - I_2)}{I_9 - I_1 + 2(I_5 - I_3 - I_7)} \right] \quad (3)$$

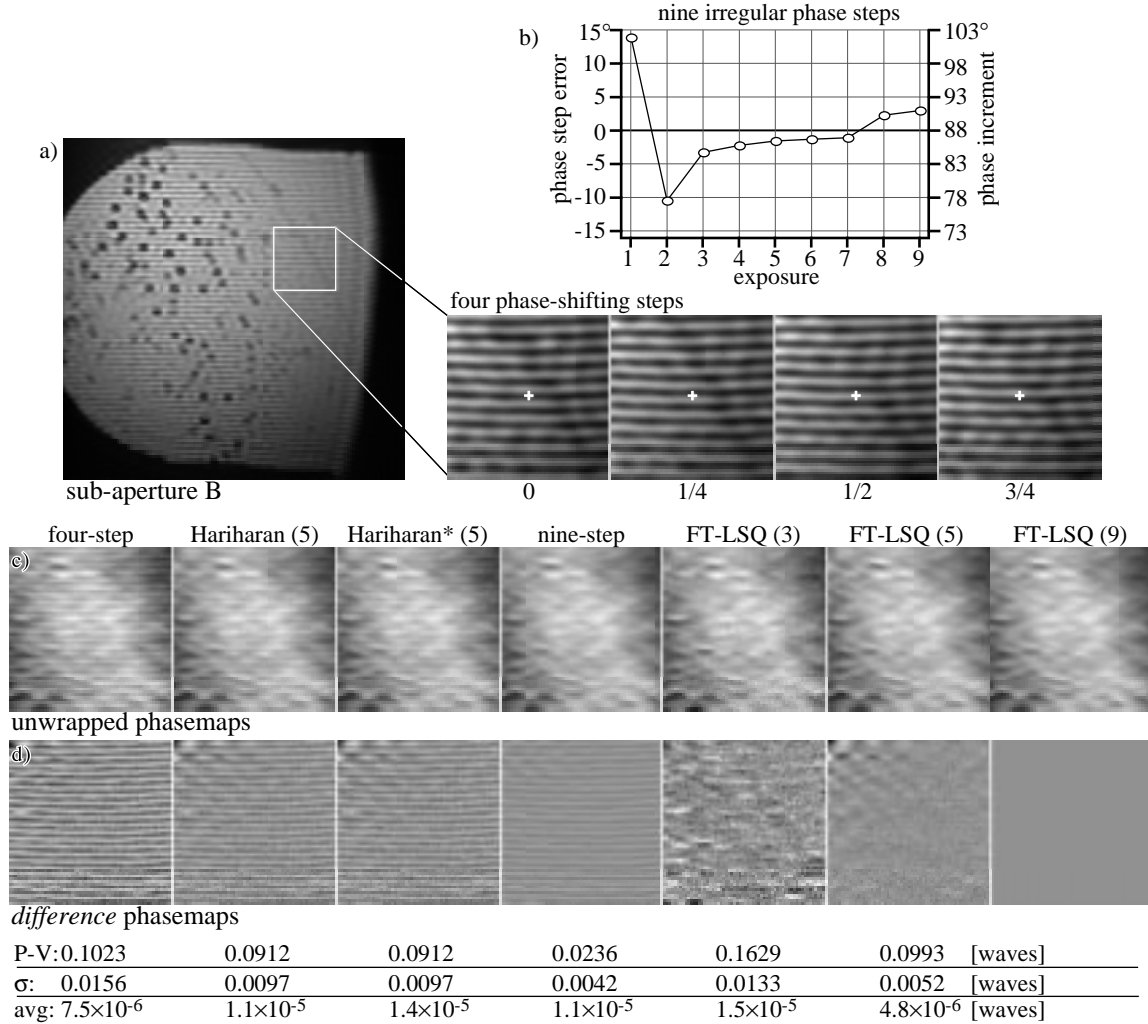


Figure 11. A number of different phase-shifting analysis techniques, including both simple methods and complex methods developed by the author, are compared in this figure. (a) 160×160 pixel details taken from a nine-exposure phase-shifting series are shown. The small white cross indicates the same stationary position in all four images. The data comes from a measurement of sub-aperture B. (b) The irregular phase-increments have an average step size of 88.0° . (c) Unwrapped wavefront phasemaps are presented for seven different methods of phase-shifting analysis. The various methods used different numbers of exposures, as indicated in the names, or parenthetically. (d) Each phasemap is compared to the nine-image least-squares phasemap, and the difference wavefronts are shown. All are plotted using the same grayscale. Displacement statistics for the six comparisons are shown below each image. Double-frequency *fringe print-through* is problematic in the application of the simple techniques. However, the complex least-squares method developed by the author to cope with irregular phase-steps is resistant to this problem.

phasemap of each of the other algorithms. In these difference images, shown in Fig. 11(d), the fringe print-through from the simple techniques and the less-regular difference patterns in the least-squares techniques are clearly visible. Below each image, the difference wavefront statistics are given.

One important statement can be made about all of these measurement techniques: the net phase-errors, or the *average* phase errors, are zero to within the measurement noise level. This is more a property of the periodicity of the fringes than of the analysis methods themselves. Depending on how the piston term is adjusted, in the absence of measurement noise the phasemaps generated by any two analysis meth-

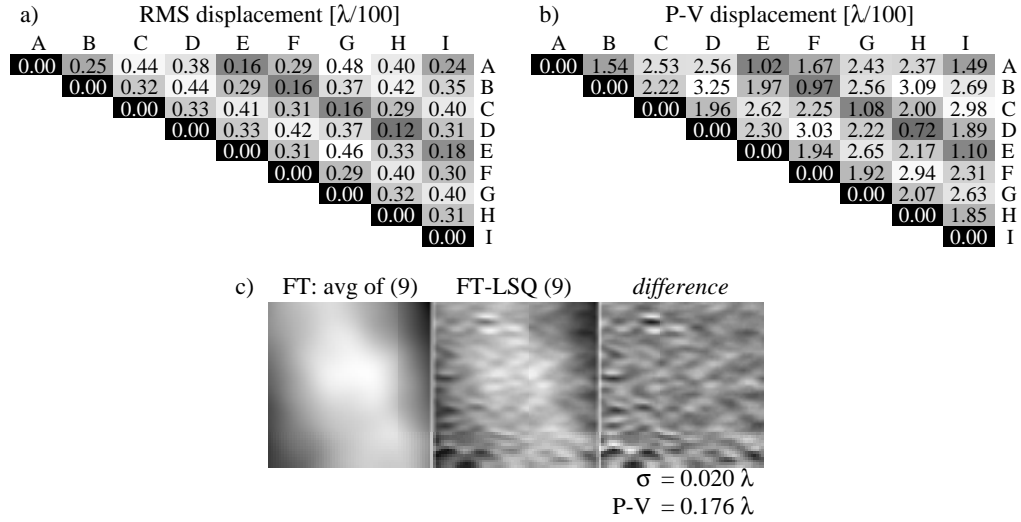


Figure 12. Analysis of the nine individual interferograms in a single phase-shifting series is performed using the Fourier-transform method. (a) and (b) Within a 160×160 pixel region, the pairs of measurements are compared to assess the self-consistency of the results. (c) The average wavefront determined from the nine individual measurements is compared to the wavefront calculated using the least-squares method. The difference wavefront reveals the extent of the spatial filtering in the Fourier-transform method, and shows the mid-spatial-frequency content of the measured phasemaps.

ods can be made to agree at one or two points within each cycle of the fringe pattern. Between these points of agreement, individual methods may diverge, as evidenced by the periodicity of the fringe print-through. The implications of this zero average difference are that in cases of high fringe density, some level of fringe print-through can be tolerated without affecting the low-spatial-frequency components of the measured phasemap. However, if the fringe density is sparse, then the phase errors introduced by print-through may dominate the low-spatial-frequency wavefront aberrations, adversely affecting the measurements.

8.10.3 Fourier-Transform versus Phase-Shifting Methods

Besides the phase-shifting methods, the other important analysis technique applied to interferometric data is the Fourier-transform method of single interferogram analysis (Section 11.3). This relies on the spatial rather than the temporal domain of measurement. Experience has shown these methods to be very reliable and robust in the presence of noise. They do, however, require the application of spatial filtering to the data and thus suffer from lower spatial-resolution than the phase-shifting methods. Furthermore, spatial filtering causes any abrupt discontinuities in the data to introduce analysis errors within the vicinity surrounding the discontinuity.

To assess the quality of the Fourier-transform method of analysis, two studies were made. The first evaluates the self-consistency of the analyses as applied separately to the nine independent measurements described in the previous section. The second compares this analysis with the least-squares technique. The Fourier-transform method is applied separately to all nine images of the phase-shifting series. To avoid possible edge-effects, the analysis is performed using the entire 1024×1024 pixel image, before the

160 × 160 pixel region of study was isolated. For this analysis, a Gaussian filter of radius seven cycles was applied in the spatial-frequency domain.

The nine separate phasemaps calculated with the Fourier-transform method were unwrapped, and the difference wavefronts from all measurement pairs were tabulated. Figures 12(a) and 12(b) show the RMS and P-V displacements of these difference wavefronts, respectively. The average of the RMS displacements is 0.0033 ± 0.0009 waves (0.044 ± 0.012 nm, or $\sim\lambda/307$).

For comparison with the least-squares phase-shifting technique, the average of the nine separate phasemaps was computed. Figure 12(c) shows a side-by-side comparison of this average wavefront with the least-squares result; both are shown with piston and tilt components removed. The difference between the two is also shown. By inspection, the characteristics of the difference clearly reveal the result of spatial filtering and averaging on the Fourier-transform data. Notice that the original fringe pattern, shown in Fig. 11(a), has horizontal fringes, indicating a *vertical* displacement of the test and reference beams in the coordinate system of this measurement. As described in Section 6.4, the overlap of the reference beam through the window causes the latter to behave as a bandpass filter for the former. For this reason, the features observable in the difference phasemap show much higher spatial-frequency content in the vertical direction than in the horizontal direction.

There are two important results here. First, the self-consistency of the Fourier-transform method applied to separate interferograms is measured to be about $\lambda/300$ on this domain. Second, the RMS difference between the Fourier-transform method and the phase-shifting analysis is approximately $\lambda/50$. That difference is comprised only of mid-to-high spatial-frequency features — features that do not significantly affect the measurement of the low-spatial-frequency aberrations of interest.

The Fourier-transform method of analysis is appropriate for use in most cases where phase-shifting data is not available or where high accuracy with high spatial resolution is not required. Further research is necessary to evaluate the performance of the Fourier-transform method in the vicinity of blemishes or near the edges of the domain, where its performance suffers.

8.10.4 Sensitivity of Least-Squares Phase-Shifting Analysis

Additional error sources in the measurements are related to the detection and digitization (discretization) of the interferogram image. In addition to photon shot-noise and noise sources in the detector's amplification electronics, the digitization performed by the detector in the recording of the interferogram should also be considered. The high-spatial-frequency noise effects all play a *very small* role in the wavefront measurements presented in this thesis; however, they may become significant in low-light interferometric applications where high-brightness sources are not available. This section is not intended to

present an exhaustive nor detailed study of noise effects, but instead to give an order-of-magnitude estimate for the ranges in which they become relevant. More detailed and general analysis of these effects has been performed by Koliopoulos (1981) and Brophy (1990).

The relationship between the phase-uncertainty of the *individual* points and the uncertainties of the Zernike polynomial coefficients is described in Section 15.6. When a large number of points N are measured (on the order of 100,000 – 300,000 is typical), the uncertainties of the Zernike coefficients are approximately $1/\sqrt{N}$ times as large as the individual variation; this may be more than 100 times smaller in ideal circumstances.

A pair of simple studies is performed to evaluate the effects of shot-noise and image digitization on the phase measurements conducted with the least-squares technique using five quarter-cycle phase-shifting steps. Here an ideal input wavefront with 20,000 points in a linear slope and a range of one cycle is used as the input. In the first study, to approximately model Poisson statistics of photon-counting the simulated intensity data with 100% fringe contrast is subjected to Gaussian noise of width \sqrt{N} . In Fig. 13, the recovered phase is compared to the input phase and the RMS difference is plotted for a range of maximum photon numbers. An empirical formula relating the RMS phase uncertainty σ_ϕ to the peak number of photons N is

$$\sigma_\phi \text{ [waves]} \approx \frac{1}{6.5\sqrt{N}}. \quad (4)$$

The digitization effect can be isolated from all of the other noise sources. Here D is an integer describing the number of discrete levels present in the fringes with no other noise sources. The RMS phase uncertainty is calculated in the same manner as above, and an empirical expression is obtained relating σ_ϕ to the level of discretization D .

$$\sigma_\phi \text{ [waves]} \approx 0.093 D^{-1} \approx \frac{1}{10.8 D}. \quad (5)$$

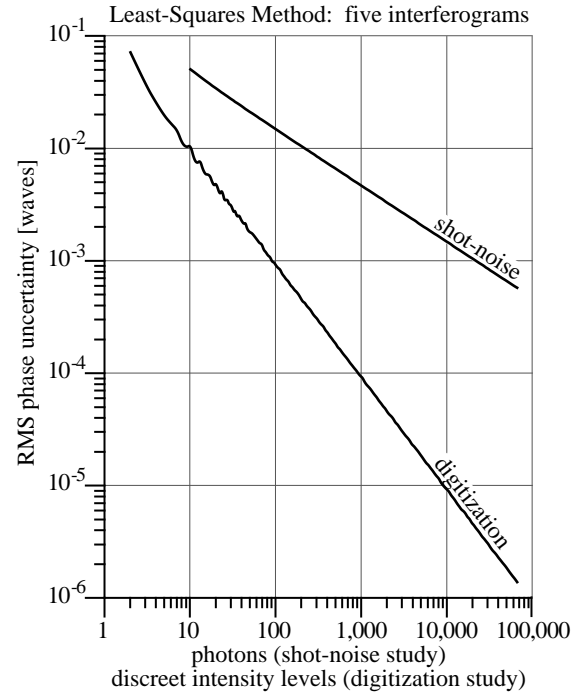


Figure 13. Two empirical investigations of the sensitivity of the least-squares method of phase-recovery to photon shot-noise and image digitization. The abscissa is given in photons for the shot-noise study, and in the number of discrete intensity levels for the digitization study.

In general, for EUV PS/PDI experiments the target fringe height is set at approximately 1000 counts. The measured detector sensitivity is 0.8 counts per detected photon. With 1000 counts, or 1250 photons, the RMS point-by-point phase uncertainty from shot-noise is approximately 4×10^{-3} waves (0.054 nm, or $\lambda/250$). Discretization with 1000 levels produces a significantly smaller RMS phase uncertainty of 9×10^{-5} waves (0.0012 nm, or $\sim \lambda/11,000$).

According to the results of this simple analysis, noise and other high-frequency random errors from the detector do not significantly affect the EUV PS/PDI measurements presented in this thesis. Once again, they may become important only when reliable data is required in low-light situations.

8.10.5 Intensity Fluctuations

Fluctuations in the overall intensity level of the recorded interferograms can introduce measurement uncertainties into phase-shifting analysis. Intensity variations can be caused by fluctuations in the light source, or by the performance of the shutter. While single-interferogram analysis methods are generally unaffected by intensity changes, phase-shifting methods rely on the stability of the system during the multiple exposures of a phase-shifting series.

Similar to the investigations presented in the previous section, a simple empirical study is performed to gauge the sensitivity of the least-squares method of phase-shifting analysis to fluctuations in the overall intensity of the measured interferograms.

Once again, an ideal input wavefront with a linear slope and a range of one cycle is used as the input. The simulated phase-shifting interference data is generated for five quarter-cycle phase-steps. Before the analysis is performed, the overall intensity levels of the individual “interferograms” are adjusted by randomly chosen multiples selected from a given Gaussian distribution width. For each distribution width of interest, 500 such analyses are performed and the RMS difference of the calculated phase from the ideal input phase is tabulated. The average of RMS phase difference indicates the expected phase-uncertainty for each intensity distribution width. The results of this investigation are shown in Fig. 14. For intensity variations below 10%, an empirical relation between the RMS phase uncertainty and the RMS overall intensity variation is

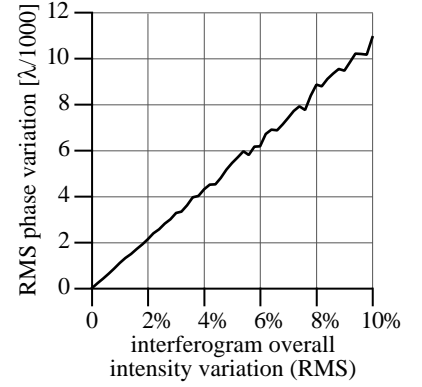


Fig 14. Fluctuations in the overall intensity of the recorded interferograms in a phase-shifting series introduce phase uncertainties into the measurement. This graph shows the results of a simple empirical study conducted to investigate this effect. Within a series of five simulated ideal interferograms, the individual exposure intensities are varied before analysis with the least-squares method is performed.

$$\sigma_{\phi} [\text{waves}] \approx 1.069 \times 10^{-3} / (\% \text{ intensity variation, RMS}) \approx \frac{(\% \text{ variation})}{936}. \quad (6)$$

In the EUV PS/PDI experiments, the primary source of overall intensity fluctuations is the steady decrease in the electron beam current of the Advanced Light Source. During a typical phase-shifting measurement, the ALS current was observed to decrease by less than 0.5%. As described previously, the beam current is recorded with each exposure, and the images are normalized before the analysis is performed. Intensity variations from the source are therefore limited to less than approximately 0.25%.

A secondary source of intensity fluctuations is the shutter, described in Section 6.2.6. The performance of the shutter used in these experiments is limited to approximately 0.02 seconds. Therefore, with a typical exposure time of five seconds, the fluctuation from the shutter could be as large as 0.4%.

These two sources of intensity fluctuations are predicted to contribute less than 0.001 waves (0.0134 nm, or $\lambda/1000$) to the phase uncertainty of the measurements — less than the variations produced by shot-noise at these intensity levels.

8.11 FRINGE CONTRAST AND WAVEFRONT FITTING UNCERTAINTY

The process of wavefront surface fitting used for the analysis of the interferometric data involves the minimization of the *fit variance* based on a finite basis of orthogonal polynomials (Chapter 15). The variance comes from the *residual* wavefront error remaining after the contribution from the polynomial surface fitting has been subtracted from the raw data. The surface fit is constructed from the contributions of each of the orthogonal polynomials in the finite basis; thus, the set of polynomial coefficients is all that is required to reconstruct the fit on a given domain. For the Zernike circle polynomials, typically 37 polynomial components are specified. As described in Section 15.6, the uncertainty in each of these fit-coefficients depends on the magnitude of the variance and on the characteristics of the individual polynomial components.

A large number of wavefront measurements were made of sub-aperture A. Over time, the transmis-

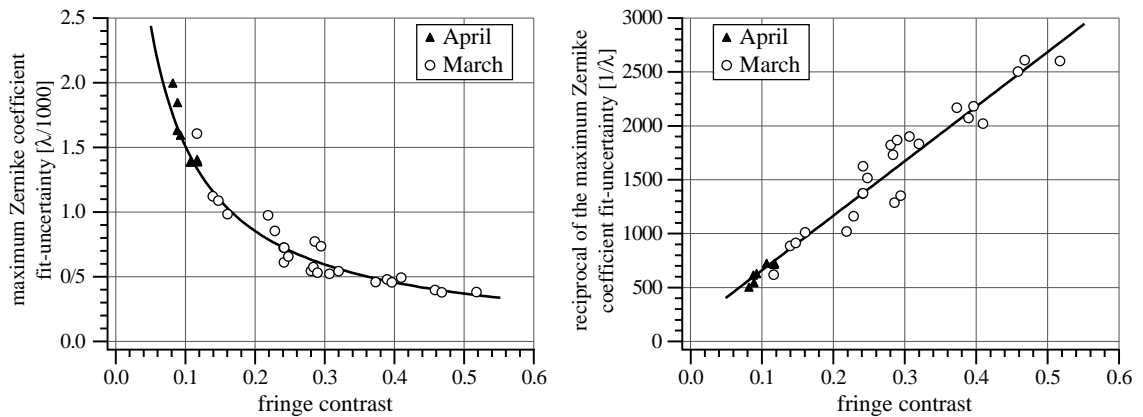


Figure 15. Measured dependence of the largest Zernike coefficient uncertainty on interferogram fringe contrast for 30 separate phase-shifting series. Each series corresponds to the same downstream field point measurement of sub-aperture A. A relative deterioration in fringe contrast observed in the April data sets may be attributable to changes in the reference pinhole transmission.

sion properties of the reference pinholes changed, and the intensity of the reference wave decreased. The loss of fringe contrast accompanying this decrease in reference wave intensity had a significant effect on the fit variance of the individual measurements.

Figure 15 shows a comparison between the measured fringe contrast (calculated with the method described in Appendix A.6) and the largest fitting-coefficient-uncertainty among the 37 Zernike polynomial coefficients, σ_{max} . Thirty phase-shifting series were considered. Note that in these measurements σ_{max} is always attributable to Zernike polynomial numbers 33 and 34, which are high-ordered coma terms. This comparison clearly demonstrates the inverse relationship between σ_{max} and the fringe contrast: the reciprocal of σ_{max} shows a roughly linear dependence on contrast. An empirical relationship that describes this dependence is

$$\sigma_{max} \approx \frac{\lambda}{160 + 5060 \text{ contrast}} . \quad (6)$$

Typically, σ_{max} is more than 1.5 times larger than the individual uncertainties of the important lower-ordered aberration components (astigmatism, coma, and spherical aberration).

Fortunately, due to the large number of points used in the fit (279,188) and the relatively high quality of the phase-shifting data available, the coefficient uncertainties related to the surface fitting are *significantly smaller* than the uncertainties related to the measurement-to-measurement variation. For this reason, the uncertainties from the surface fitting are not included in the analysis presented in Section 7.2.4.

8.12 SUMMARY AND CONCLUSIONS

All of the individual experiments described in this chapter demonstrate the precision of the interferometer: reference and object pinhole displacement experiments, mechanical stability tests, pinhole exchange, system re-alignment, and observation of the geometric coma systematic error. All describe experiments that are similar in principle, where two wavefronts are compared by inspection of their differences. Here, the *variations* in the data stand out and are characterized.

The following section contains a brief summary of the main performance evaluation experiments described in this chapter. Following that is a discussion of accuracy and the need for further testing.

8.12.1 Summary of Precision-Testing Measurements

- **8.2 Reference pinhole spatial filtering.** Based on measurements made as the reference pinhole is displaced slightly from the optimum position, the expected measurement-to-measurement RMS wavefront variation is 0.019 ± 0.009 waves (0.249 nm, or $\sim\lambda/53$).
- **8.3 Object pinhole spatial filtering.** In two experiments, lateral translation of the object pinholes produced an RMS wavefront variation of 0.006 ± 0.001 waves (0.082 ± 0.018 nm, or $\sim\lambda/164$) in the first experiment, and 0.014 ± 0.005 waves (0.192 ± 0.065 nm, or $\sim\lambda/70$) in the second.
- **8.4 Through-focus experiments.** Small longitudinal translations of the object pinhole adjust the posi-

tion of the reference pinhole through focus. The average of the measured RMS displacements of the difference wavefronts is 0.015 ± 0.007 waves (0.204 ± 0.088 nm, or $\sim\lambda/66$).

- **8.5 Mechanical stability.** Based on observations of the wavefront changes over ten minutes as the system is held stationary, the interferometer components appear to drift. The image-plane lateral and longitudinal drift rates were approximately 9.0 nm/min and 7.2 nm/min respectively. On the object-side of the optic, these motions would be 90 nm/min laterally and 0.72 μ m/min longitudinally.
- **8.6.1 Object pinhole exchange and measurement repeatability.** Five object pinholes were tested in measurement of sub-aperture A. The average of the measured RMS displacements of the difference wavefronts is 0.015 ± 0.004 waves (0.197 ± 0.051 nm, or $\sim\lambda/68$).
- **8.6.2 System re-alignment.** The test optic was removed from the vacuum chamber and re-aligned from scratch several times. For the two combined measurements of sub-aperture A, the RMS displacement of the difference wavefront is 0.018 waves (0.24 nm, or $\sim\lambda/56$).
- **8.8 Zeroth-order reference versus first-order reference.** A comparison of the two methods shows an average difference wavefront of RMS displacement 0.010 ± 0.003 waves (0.13 ± 0.04 nm, or $\sim\lambda/101$).
- **8.11 Fringe contrast and wavefront fitting uncertainty.** A dependence was observed between the measured fringe contrast and the coefficient uncertainties of the Zernike polynomial fit. The largest observed uncertainty of the first 37 coefficients follows $1/\sigma_{max} [1/\text{waves}] \approx 160 + 5060 \text{ contrast}$, for contrast values between 10% to 50%. Uncertainties of the low-ordered primary aberrations are approximately two-thirds as large. Typical values range from $2\text{--}7 \times 10^{-4}$ waves ($2.7\text{--}9.4 \times 10^{-3}$, or $\sim\lambda/5000\text{--}\lambda/1400$).

8.12.2 Comments

It is clear from the above measurements that the most significant limitation to the measurement precision is the quality of the reference wavefronts generated by the reference pinhole. Every one of the tests described here incorporates a re-alignment (large or small) or other change that causes the reference pinhole effects to be included in the measurement. Not doing so is unavoidable. By isolating these reference pinhole effects, the reference pinhole spatial filtering experiment indicates that measurement variations on the order of $\lambda/50$ RMS should be anticipated.

One of the four pinholes, pinhole C, was found to introduce the largest measurement-to-measurement variation and the least spatial filtering of the four pinholes studied. Yet this pinhole is not much larger than the other pinholes used for these experiments. Here, two conclusions can be drawn: the reference pinhole is the most significant limiting agent in achieving high measurement precision in the EUV PS/PDI; and improvement could be achieved by the use of slightly smaller pinholes. A small sacrifice in fringe contrast brought about by the use of a smaller reference pinhole will not significantly limit the precision of the measurements relative to the other contributing factors.

8.13.3 The Astigmatism Problem

The goal of having an interferometric system for which the accuracy and precision can be specified independently from the characteristics of the optical system under test appears to be thwarted by the diffi-

culty of spatially filtering astigmatism. Without exception, the dominant component of the difference wavefronts in each of the relevant experiments described in this chapter is astigmatism.

Section 4.6.2 gives some insight as to how astigmatism becomes the most difficult aberration to remove by spatial filtering, but it does not provide insight into any one solution more effective than reducing the pinhole size. It appears clear both experimentally and from the simple model that the pinhole size standard for filtering astigmatism is narrower than for any of the other primary aberrations. For this reason, the performance of the system necessarily depends on the constituent aberrations of the test optic.

8.13.4 Accuracy and the Need for Two Pinhole Tests

In addition to *high precision*, *high accuracy* is the true goal of interferometric optical system measurement.

In principle, the simple *difference measurements* described in this chapter, in which the system is subjected to slightly different conditions in two measurements, are incapable of detecting systematic errors. The presence of a systematic wavefront figure error would go unnoticed if it were lost in the subtraction of the two measurements being compared.

When the assumption is made that every optical component of the interferometer is capable of contributing systematic errors, then a wide variety of systematic effects and the mechanisms to generate them can be hypothesized. As discussed in Section 5.8, systematic errors introduced directly by defects in the grating beamsplitter can be identified by large translations of the grating, or by grating exchange. More onerous by far are reference wave systematic errors introduced by the object and image-plane spatial filter pinholes. It may be suggested that the particular defects or irregularities of a given pinhole introduce a stable aberration pattern in the reference wavefront it generates. In addition, there may be unknown physical properties of pinhole diffraction (e.g. polarization dependent astigmatism, irregularities caused by non-uniform illumination, etc.) that may create systematic errors of significant magnitude near the target accuracy. Far more simple are geometric systematic errors (Chapter 5) that come from the beam separation (geometric coma), detector misalignment (a source of astigmatism), the use of a planar grating in a spherical beam (grating coma), and the use of a planar detector in a spherical beam (a source of radial distortion).

While some of these systematic effects can be observed and are easily subtracted from the wavefront measurements (e.g. geometric coma), others present a more daunting problem. The importance of identifying these effects cannot be overstated because the accuracy of the interferometer is at stake.

One strategy for overcoming the systematic errors uses a two-pronged approach. First, of the systematic errors that cannot be directly observed, can their *magnitude* be determined? This is the strategy applied to the investigation of the pinhole spatial filtering. For example, what may be manifest as a systematic error in a single measurement becomes a random error when a large number of measurements are

made in ways that induce changes in the “systematic” error. The pinhole translation and pinhole exchange experiments are all examples of this strategy for turning systematic errors into random errors and identifying their magnitude by carefully observing *differences*. The average magnitude of the differences indicates the typical contribution of the systematic error to any single measurement.

The second strategy is to find a way to isolate the systematic effects under consideration. The geometric coma removal is one example of this. Given that the systematic error depends directly on the magnitude and direction of the beam separation, introducing a 90° rotation in the beam separation allows this systematic effect to be identified and quantified.

The identification and isolation of other systematic errors requires a so-called *null test*. In such, every attempt is made to remove the contributions of the test optic from the measurement, and the bare system performance is studied. One way in which this could be achieved in the EUV PS/PDI is by using a *two-pinhole test*, in which a two-pinhole spatial filter is placed in the image plane of the PS/PDI (Goldberg 1997). The image-plane window that transmits the test beam is replaced by a second tiny reference pinhole. The measured interference pattern and wavefront can be compared to those predicted for two ideal pinhole spatial-filters, and systematic errors will be revealed in the difference. Besides the expected tilt and geometric coma, small detector misalignments may be observable in this sensitive technique.

To improve the measurements and broaden the significance of the two-pinhole test, the experiment may be expanded to include a large number of pinhole pairs, in different orientations, and with different separations. Sensitivity to certain geometric errors will be greater in some orientations than in others. In addition, the use of many pinhole pairs provides information on the variation in the spatial filtering properties of the pinholes: the waves diffracted from the pinholes are essentially being “compared” with each measurement.

Some effects may not be observable using the two-pinhole tests. For example, if every pinhole were to create the same kind of aberration in the diffracted reference wave it generates, then a comparison of any two waves by subtraction would reveal nothing. Experiments have been performed to assess the quality of a single reference wave, using shearing techniques to compare the wavefront to an angularly displaced copy of itself. Such measurements could be attempted for the PS/PDI reference waves, but it is not clear that the tests could achieve the desired $\text{sub-}\lambda/100$ accuracy that is necessary. Alternatively, rotation of the optical system may help to identify these effects.

9

Chromatic Effects

9.1 INTRODUCTION: 10× SCHWARZSCHILD MULTILAYER COATING PROPERTIES	168
9.2 WAVELENGTH-DEPENDENCE OF THE TRANSMITTED INTENSITY	168
9.3 WAVELENGTH-DEPENDENT WAVEFRONT MEASUREMENTS – CHROMATIC ABERRATIONS	169
9.4 BROADBAND ILLUMINATION	170
9.4.1 Wavefront Measurements with <i>Broadband Illumination</i>	
9.4.2 Wavefront and Intensity Measurements in the Zeroth-Order Reference Configuration	
9.5 VISIBLE-LIGHT	171

9.1 INTRODUCTION: 10× SCHWARZSCHILD MULTILAYER COATING PROPERTIES

Measurements of isolated chromatic effects provide perhaps the clearest demonstration of the sensitivity and importance of at-wavelength interferometric testing. The resonant reflective multilayer coatings exhibit a strong wavelength-dependent response in both reflected intensity and phase that occurs separately from the figure of the optical surfaces under test. By tuning the wavelength and performing measurements near the reflectivity peak, these chromatic effects are easily demonstrated and the properties of the multilayers can be studied.

Multilayer response depends critically on the multilayer period, the illumination angle, and the wavelength and polarization of the incident light. As described in Section 6.2.1, the multilayer-coatings are designed for peak reflectivity and wavefront response at 13.4-nm wavelength. The range of angles subtended by the light incident on the primary mirror necessitates the use of a multilayer containing a radial thickness gradient. This design makes the performance of the system very sensitive to changes in wavelength.

This chapter contains measurements of the chromatic response of the multilayer coatings. In addition to the direct demonstration of chromatic aberrations and the sensitivity of the interferometer itself, measurements such as these would be required to understand the system performance in the presence of broadband illumination. For example, understanding imaging performance under broadband illumination requires that both the intensity transmission and the wavefront be considered over the range of illumination wavelengths. A separate section of this chapter addresses measurements made without the wavelength-filtering of the monochromator.

Qualitative wavelength-dependent measurements of chromatic aberrations have been reported previously by Ray-Chaudhuri (1995a). The investigations presented here may be the first high-precision quantitative measurement of such effects.

9.2 WAVELENGTH-DEPENDENCE OF THE TRANSMITTED INTENSITY

The first experimental indications of the presence of chromatic effects related to the multilayer coatings were observable in the transmitted intensity patterns. Figure 1 shows the transmitted intensities for sub-apertures A, B, and C. The data from sub-aperture C were recorded with the sub-aperture defining pupil removed and a large region of the clear aperture visible. These images clearly show the response of the multilayer coatings in a wavelength-dependent, annular pattern. As described in Section 6.2.2, for these measurements the illumination bandwidth set by the monochromator is measured to be below 1-Å full-width at half-maximum.

The areas at the inner and outer edges of the annulus are especially interesting. The periods of the multilayer coatings were designed and measured to be within a thickness tolerance of 0.125 Å over a

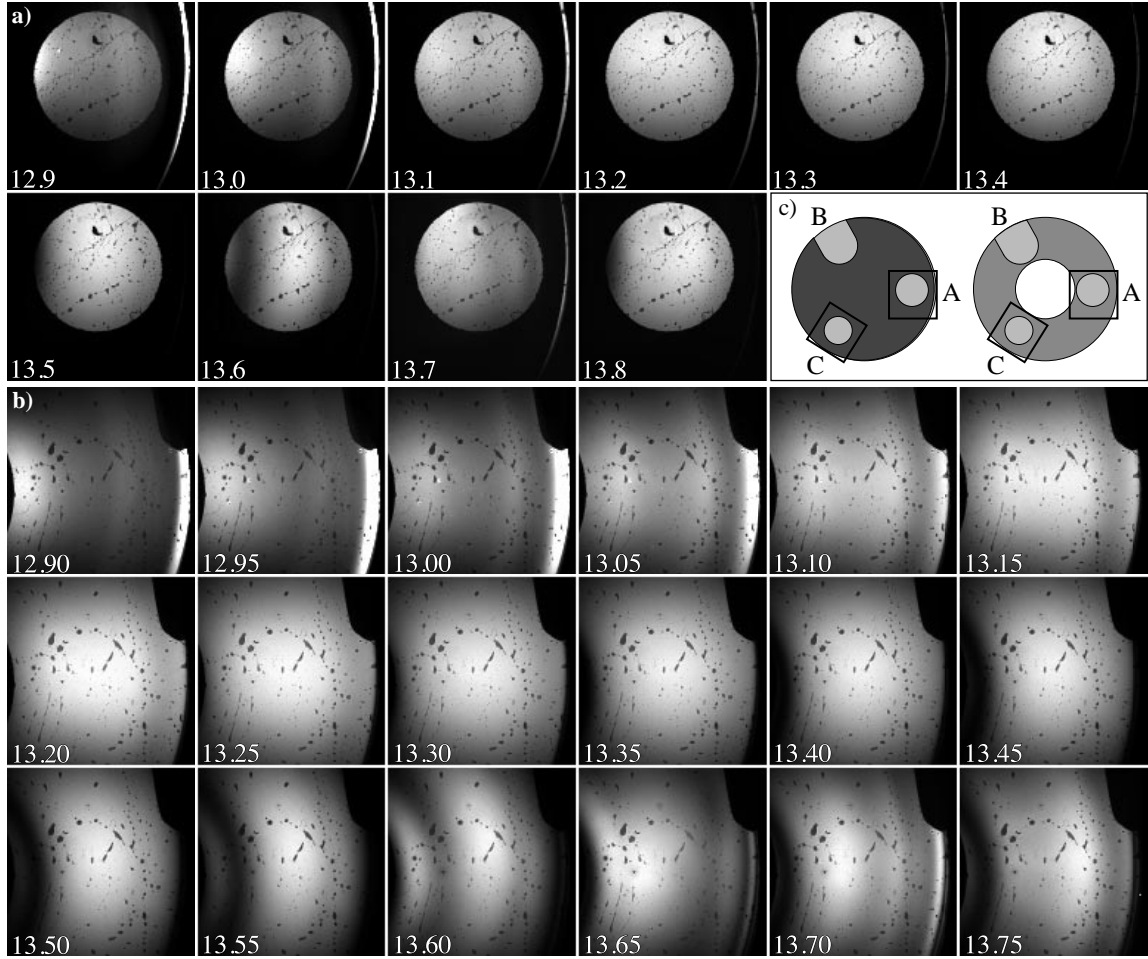


Figure 1. Wavelength-dependent intensity transmission patterns are shown for two sub-apertures of the 10 \times Schwarzschild objective. (a) Sub-aperture A (0.07 NA) is shown with the aperture-defining stop in place. (b) Sub-aperture C is shown with the stop removed to expose a larger section of the annulus. Illumination wavelengths in nanometers are shown in the lower-left corner of each image. (c) The appearance of the Schwarzschild objective's full annular pupil, with and without the stop, is shown. The square outlines illustrate which two sections of the annulus are shown in (a) and (b). The annular characteristics of the multilayer response are clearly visible in these images.

finite region of the aperture (i.e. a limited range of radii). At the edges where no effort was made to control the period, the reflectivities appear highest at the shorter wavelengths; this indicates *thinner* layers in these regions. Comparison of the measured and theoretical intensity transmission behaviors has been presented elsewhere (Tejnil 1997).

9.3 WAVELENGTH-DEPENDENT WAVEFRONT MEASUREMENTS – CHROMATIC ABERRATIONS

When the PS/PDI is aligned and optimized, experiments to measure the wavelength dependence of the wavefront are very simple to perform: adjustment of the undulator and beamline monochromator tune the illumination wavelength; *very* minor position optimization of the optical components is all that is

Table 1. The wavefront measured at the central wavelength, 13.4 nm, is subtracted from the individual wavefronts measured at each wavelength generating the *difference wavefront*. Statistics of the difference wavefronts are given. The measured change of the focal position is also given.

λ [nm]	P-V [nm]	RMS [nm]	defocus [μm]
13.0	1.70	0.29	1.54
13.1	1.36	0.17	1.62
13.2	1.02	0.13	1.55
13.3	0.48	0.07	0.09
13.4	—	Central wavelength	—
13.5	1.65	0.17	0.79
13.6	3.28	0.48	1.28
13.7	2.58	0.34	1.24

required to perform measurements at different wavelengths.

The wavelength-dependent change of the measured wavefronts is a small effect. Its significance becomes most apparent in an examination of the *difference wavefronts* generated by comparison to the wavefront at 13.4-nm wavelength. With the wavefronts scaled in nanometers (rather than in waves), pairs of measured wavefront profiles are compared. The measured wavefronts from sub-aperture A are reconstructed from the first 37 Zernike polynomials to isolate the low-spatial-frequency figure changes of interest.

The difference wavefronts are shown in Fig. 2. In Fig. 2(a), the difference wavefronts are individually scaled from black to white. In 2(b), the eight difference wavefronts are all represented on the same grayscale. The relevant statistics of these difference wavefronts are presented in Table 1. One noteworthy effect is the apparent change in the focal position at each wavelength. On either side of the central wavelength (13.4 nm), the focal shift occurs in the same longitudinal direction. Defocus is not included in the difference wavefronts of Fig. 2 or in the wavefront statistics reported in Table 1.

9.4 BROADBAND ILLUMINATION

To illuminate the system with relatively broadband illumination, the monochromator's planar grating may be

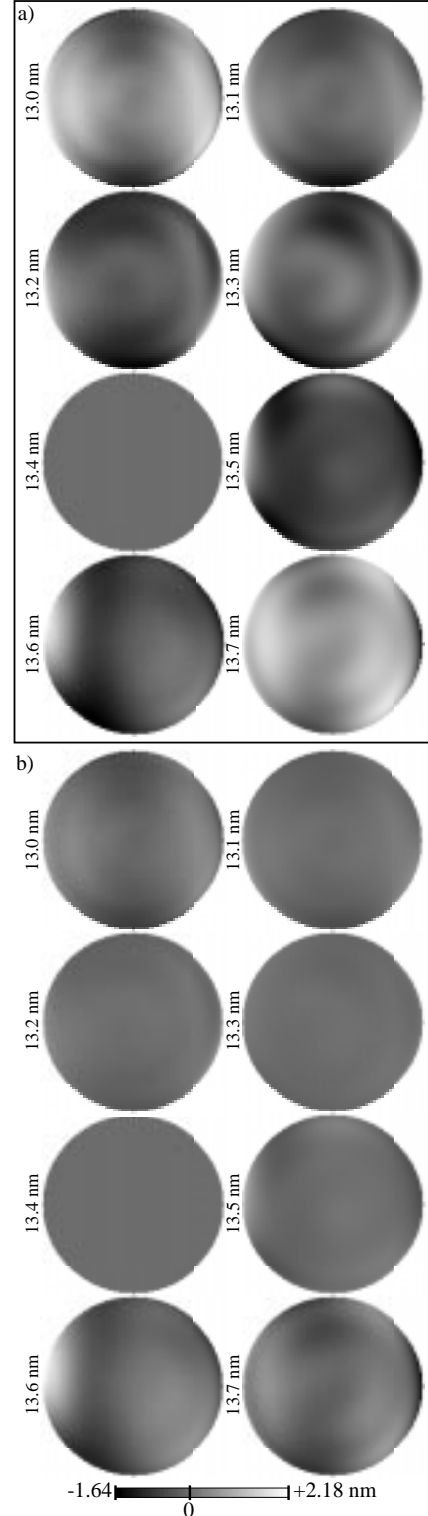


Figure 2. Chromatic aberrations are observable in the variation of the difference wavefronts measured over a range of wavelengths. These are generated by comparison of the wavefronts to the wavefront measured at the design wavelength, 13.4 nm. (a) individually scaled images. (b) all wavefronts are shown on the same scale grayscale.

adjusted to give a specular (zeroth-diffractive-order) reflection. In this configuration, the bandwidth is primarily determined by the undulator: with 55 magnetic periods, the natural bandwidth of the undulator radiation into the first harmonic is $\lambda/\Delta\lambda \approx 55$, or 0.24 nm at 13.4-nm wavelength. The total flux reaching the K-B mirrors does not increase noticeably because the blazed grating diffracts very efficiently into its first diffractive order.

With a measured bandwidth of 0.9 nm (6.7%), the near-45° multilayer-coated turning mirror does not significantly filter the beam. Here, the term *broadband* is used to denote the case where the zeroth-order reflection from the monochromator is used — not to indicate the presence of *truly* broadband light.

A series of interferometric experiments was performed with the beamline in this *no monochromator* configuration. The experiments were all conducted using sub-aperture C (0.06 NA) of the Schwarzschild objective. Experiments with the standard beamline configuration, using the first diffractive order from the monochromator, were conducted immediately following the broadband experiments, with no physical changes made to the interferometer.

9.4.1 Wavefront Measurements with Broadband Illumination

Comparison of the wavefront data measured both with and *without* the monochromator shows agreement to well within the expected uncertainty. The wavefront in the *no monochromator* case was calculated from three phase-shifting series. Compared to the measured wavefront at 13.4-nm wavelength, the difference wavefront, reconstructed from the first 37 Zernike polynomials, shows an RMS wavefront displacement of 0.011 waves (0.147 nm, or $\sim\lambda/90$) and peak-to-valley displacement of 0.108 waves (1.45 nm, or $\sim\lambda/9$). Based on these values, the two measurements are indistinguishable within the uncertainties typically observed in this interferometer.

9.4.2 Wavefront and Intensity Measurements in the Zeroth-Order Reference Configuration

In the presence of broadband illumination, the zeroth-order reference configuration of the PS/PDI is predicted to behave differently from the default first-order reference configuration. As described in Section 5.4, the wavelength-dependent diffraction angle of the grating beamsplitter separates the available wavelength components laterally in the image-plane. The position of the zeroth-order focus remains stationary, affected only by the chromatic aberrations in the test optic. Yet in the first-order reference configuration, where the pinhole sits in the grating's first-order beam, it functions as a monochromator — based on the geometry, it transmits some wavelength components more efficiently than others. The test beam is transmitted through the window and may contain a much broader bandwidth than the reference beam. Alternately, in the zeroth-order reference configuration the various wavelength components are not distributed laterally in vicinity of the reference pinhole, and (dependent on the chromatic aberrations of the test optic) the reference beam is broadband. The test beam in this configuration *also* contains the available

wavelength components, transmitted through the large window.

With broadband illumination, a comparison is made of the wavefront measurements from these two configurations. The two tests were performed consecutively; wavefront measurements from single phase-shifting series are compared here. The difference wavefronts, compared assuming 13.4-nm central wavelength, show an RMS displacement of 0.010 waves (0.134 nm, or $\sim\lambda/100$) and P-V displacement of 0.122 waves (1.635 nm, or $\sim\lambda/8$). Hence, the wavefront measurements are again indistinguishable within the typical uncertainties.

From these two configurations, the transmitted intensity is expected to be higher in the first-order reference configuration because *all* of the wavelength components of the test beam are transmitted to reach the detector. The fringe contrast is affected by three independent considerations: the relative intensity of the first-order beams is estimated to be approximately 40% of the zeroth-order beam; the spatial filtering of the reference pinhole significantly reduces the intensity of the reference beam; and, since interference fringes are only produced by the interference of like-wavelength components, a mismatch of the bandwidths of the two beams reduces the observed fringe contrast. Given these considerations, the zeroth-order reference configuration may be expected to produce greater fringe contrast.

After compensating for the decreasing intensity of the synchrotron illumination, the total measured signal is 2.4 times higher in the first-order reference than in the zeroth-order reference configuration. The overall fringe contrast is measured to be 22% with the first-order reference, compared to 41% with the zeroth-order reference configurations.

These particular intensity and fringe contrast measurements depend too strongly on the transmission properties of the reference pinhole to carry broad implications for the benefits of one configuration over the other. Furthermore, the quality of the optical system plays an important role in determining the maximum achievable fringe contrast from the PS/PDI. More investigation is needed to establish the advantages and disadvantages of these two arrangements. However, the consistency among the wavefront measurements indicates that the interferometer system is very tolerant of the bandwidth of the illumination.

9.5 VISIBLE-LIGHT

Observations of the intensity transmission of the 10× Schwarzschild objective were made at visible-light wavelengths. As described in Section 6.2.3, HeNe laser light was introduced via a fiber-optic line directly into the HMF. Spatial filtering was performed by the fiber's polished tip, and the illumination over-filled the NA significantly. The intensity transmission data is shown in Fig. 3 adjacent to a similar EUV image at 13.4-nm wavelength.

A special visible light PS/PDI image-plane pinhole membrane was fabricated, and one series of

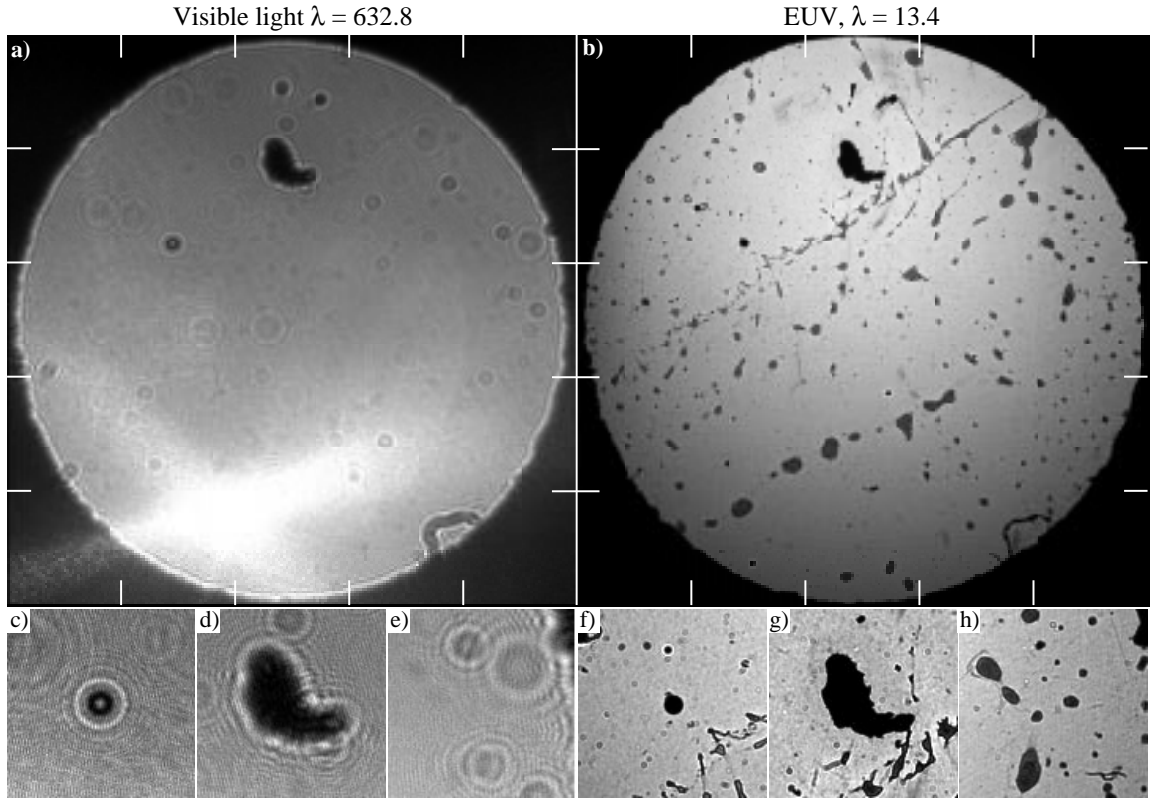


Figure 3. Side-by-side comparison of the transmitted intensity measured at a visible-light wavelength (a), 632.8 nm, and the EUV design wavelength (b), 13.4 nm. Three regions are shown in detail for visible-light, (c) through (e), and for EUV, (f) through (h). The detector is well beyond the plane in which the pupil is re-imaged by the secondary, and diffraction affects the two wavelengths to a much different extent. Only some of the blemishes observable at EUV wavelengths are seen in the visible light image, demonstrating important differences in these two methods of inspection. The bright patch of light in the lower portion of the visible-light image is caused by an unintentional reflection in the vacuum chamber.

experiments was conducted as a demonstration of PS/PDI interferometry at visible-light wavelengths. Because of the large diffraction angles from the grating beamsplitter used in the EUV experiments, a coarser grating was chosen. This ensures that the zeroth- and first-order beams fall within the acceptance angle of the object-side NA and reduces the fringe density in the interferogram. In these experiments, a simple mechanical limitation prevented the fiber-tip from reaching the object plane. As a result, the measurements were hampered by an unacceptable amount of defocus. Figure 4 shows one interferogram pat-

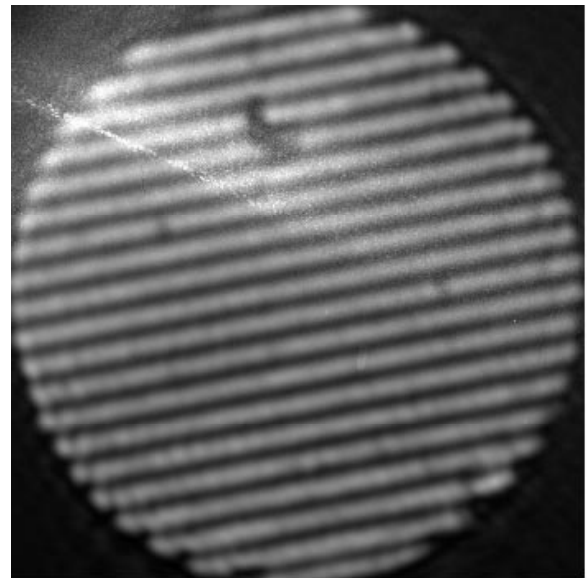


Figure 4. A visible-light PS/PDI interferogram of sub-aperture A. The grating beamsplitter used in this image is more coarse than the one used for EUV interferometry, leading to a lower fringe density.

tern from this demonstration experiment.

The development of a concomitant capability high-accuracy visible-light interferometry capability is highly desirable for many reasons. System alignment could be performed while the components inside the chamber are accessible, before the system is brought under vacuum. Furthermore, direct comparisons could be made between the wavefront measurements performed at EUV and visible wavelengths.

One major difficulty in this effort is the presence of systematic errors that depend on the image-plane beam separation. For example, the magnitudes of the systematic coma effect (Section 5.5) and the astigmatism related to detector alignment (Section 5.6) depend linearly on this separation. At nearly fifty times the EUV wavelength, the beam separation required for the visible-light measurements makes these systematic effects more than an order of magnitude larger than the small aberrations of interest. Further research is required to identify ways to address these problems. One solution may be to use a different common-path interferometer, such as the LSI (Chapter 4) or the conventional PDI, both of which are easier to develop and operate at visible-light wavelengths than for the EUV.